Application of a Patched-Grid Algorithm to the F/A-18 Forebody-Leading-Edge Extension Configuration

James L. Thomas*
NASA Langley Research Center, Hampton, Virginia
Robert W. Walters†
Virginia Polytechnic Institute and State University, Blacksburg, Virginia
Taekyu Reu‡
Florida State University, Tallahassee, Florida
Farhad Ghaffari§
Vigyan Research Associates, Hampton, Virginia
and
Robert P. Weston¶ and James M. Luckring¶
NASA Langley Research Center, Hampton, Virginia

A patched-grid algorithm for the analysis of complex configurations with an implicit, upwind-biased Navier-Stokes solver is presented. Results from both a spatial-flux and a time-flux conservation approach to patching across zonal boundaries are presented. A generalized coordinate transformation with a biquadratic geometric element is used at the zonal interface in order to treat highly stretched viscous grids and arbitrarily shaped zonal boundaries. Applications are made to the F/A-18 forebody-leading-edge extension configuration at subsonic, high-alpha conditions. Computed surface flow patterns compare well with ground-based and flight-test results; the large effect of Reynolds number on the forebody flowfield is shown.

Nomenclature

a_{1-8}	=	coefficients for surface definition
$\bar{c}$	=	mean aerodynamic chord
F, G, H	=	flux vectors (convective and pressure terms)
H_v	=	flux vector (viscous terms)
M_∞	=	freestream Mach number
Q	=	time-flux vector
r	=	position vector
$R_{\bar{c}}$	=	Reynolds number based on $\bar{c}$
t	=	time
x,y,z	=	Cartesian coordinates
y^+	=	turbulent inner law variable
α	=	angle of attack, deg
ξ,n,ζ	=	body-fitted coordinates

Introduction

THERE is an increasing effort in the development and application of Euler/Navier-Stokes computational algorithms for realistic aircraft configurations. Use of these prediction tools, in combination with ground-based and flight experiments, can significantly reduce the required time and cost of the design cycle. Timeliness is a critical issue in the design cycle and there is a pressing need to reduce the overall time required for an analysis of candidate configurations that might arise in a typical design cycle.

The flow solvers in use today can be loosely classified into three types according to the underlying grid topology: 1) Cartesian, 2) unstructured, and 3) multiblock structured. The Cartesian-grid solvers lead to the simplest algorithms with the fewest operations and smallest memory requirements per grid point but are least efficient and accurate in applications to curved surfaces. With the latter two approaches, the use of body-conforming meshes leads to straightforward treatment and accurate resolution of general surfaces. The unstructured mesh solvers are the most general algorithms and their principal advantage is that grids over complex geometries can be generated in the shortest time period. However, these algorithms are also the most costly in terms of operations per time step and memory per grid point because of nonsequential memory access and the explicit connections required between the cells of the mesh.

The multiblock-structured meshes are more efficient in terms of operation count and memory than the unstructured meshes because general connection information is restricted to the edges of the blocks. However, more constraints are placed on the grid generation process in each block, although there is an active body of ongoing research to reduce or eliminate many of these constraints. The structured-mesh approach leads to the most efficient algorithms for treating viscous flows, as the grids can be highly stretched in the direction normal to the developing shear layers.

The present work is directed toward the development of improved techniques associated with the block-structured approach, and, in particular, the patched-grid approach. In this method, also referred to as a domain decomposition method, the computational domain is divided into a number of zones or blocks, each of which models the local geometric features and requisite physics of the configuration.[1-8] The grids in each zone can be determined independently, with the net result that the grid generation task is simpler and the solution is more efficient, since local clustering of the grid cells to resolve geometric and physical features in one region need not propa-

Presented as Paper 89-0121 at the AIAA 27th Aerospace Sciences Meeting, Reno, NV, Jan. 9-12, 1989; received April 10, 1989; revision received Dec. 14, 1990.

*Senior Research Scientist. Associate Fellow AIAA.
†Associate Professor. Member AIAA.
‡Assistant Research Scientist.
§Research Engineer. Senior Member AIAA.
¶Research Engineer. Associate Fellow AIAA.

gate to other blocks. The utility of the approach in a longitudinally patched-grid framework for an F-18 and an SR-71 configuration at supersonic speeds has been demonstrated previously for inviscid flow.[2,3] The method is extended in the present work such that the patching plane can be a general three-dimensional surface. The extension also overcomes a problem encountered in the application to viscous flows in which a highly stretched grid is present on either side of a zonal interface.

Two approaches are described for maintaining the accuracy of the solution across the zonal interface. Applications using the two patching algorithms are made to the F/A-18 aircraft, at subsonic high-alpha conditions, as part of an ongoing high angle-of-attack research program being conducted by NASA. Computed surface flow patterns from solutions to the Navier-Stokes equations at $\alpha = 30$ deg are compared to the results from ground-based experiments conducted at NASA Langley and from in-flight experiments conducted at NASA Ames-Dryden using the High Alpha Research Vehicle (HARV).[9] The results are used to understand better the low Reynolds number ground-based tests, which are laminar and transitional, and their relationship to the flight results. A comprehensive comparison at $\alpha = 20$ deg, including surface pressure comparisons, is given by Ghaffari et al.[10]

Single-Zone Algorithm

The governing equations are the time-dependent Reynolds-averaged compressible Navier-Stokes equations, cast in conservation law form and generalized coordinates as

$$\frac{\partial \hat{Q}}{\partial t} + \frac{\partial \hat{F}}{\partial \xi} + \frac{\partial \hat{G}}{\partial \eta} + \frac{\partial (\hat{H} - \hat{H}_v)}{\partial \zeta} = 0 \tag{1}$$

expressing the conservation of mass, momentum, and energy. The superscript ^ denotes a quantity in generalized coordinates. The thin-layer form of the equations is used, where ζ is the coordinate normal to the body surface. An ideal gas is assumed; the effect of turbulence is accounted for through the concepts of eddy viscosity and eddy conductivity. The algebraic turbulence model of Baldwin and Lomax[11] is used to evaluate the turbulence quantities, including the modifications introduced by Degani and Schiff[12] to ensure that the proper length scales are used in separated vortical flows.

The equations, although written in generalized coordinates, are solved with a semidiscrete finite-volume algorithm, resulting in a consistent approximation to the conservation laws in integral form.[10,13,14] The convective and pressure terms are differenced with the upwind flux-difference-splitting technique of Roe.[15] The MUSCL (Monotone Upstream-Centered System of Conservation Laws) approach of Van Leer[16] is used to determine state-variable interpolations at the cell interfaces. Each flux computation requires a single point on each side of the interface for first-order spatial differencing and two points on either side of the interface for the third-order upwind-biased spatial differencing used here. The shear stress and heat-transfer terms are differenced centrally.

The equations are advanced in time to the steady state in delta form so that the steady state is independent of the time step. Two implicit algorithms are used: 1) a spatially factored diagonalized algorithm,[13] or 2) a hybrid algorithm, using streamwise relaxation and approximate factorization in the crossflow planes.[2]

Patching Algorithm

General Concepts

The two general approaches considered for patching across zonal grids with coincident boundaries can be addressed using the sketch in Fig. 1. Two-dimensional Cartesian grids in two zones are shown; the two zones have uniform spacing in the x direction and a grid mismatch in the y direction. The indices

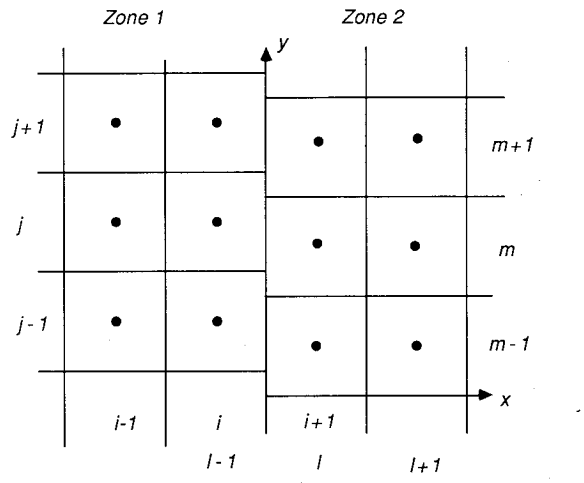

Fig. 1 Two-dimensional zonal interface.

(i, j) refer to the cell-center locations of zone 1 and (l, m) to those of zone 2. The zonal interface across which the solution must be patched corresponds to the points defined as $\{x_{i+1/2}, j; j = 1, j_{\max}\}$ and $\{x_{l-1/2,m}; m = 1, m_{\max}\}$.

Defining the spatial flux in the x direction as F, Rai[1] has demonstrated that global conservation can be maintained by enforcing spatial-flux conservation along the interface, as

$$\int \boldsymbol{F}^{(1)}(x_{i+1/2})\, dy = \int \boldsymbol{F}^{(2)}(x_{l-1/2})\, dy \tag{2}$$

The flux in zone 2, say, is constructed from the flux in zone 1 so that Eq. (2) is satisfied. For a scheme requiring two points on either side of the interface to compute the flux, the required flux in zone 1 can be constructed from the data in zone 1 and an interpolation of zone 2 data at points defined by a projection of zone 1 into zone 2. Referring to the conserved variables Q as the time flux of mass, momentum, and energy, much as F is referred to as the spatial flux of mass, momentum, and energy, the conservation of time flux can be expressed as

$$\iint \boldsymbol{Q}^{(1)}\, dx\, dy = \iint \boldsymbol{Q}^{(2)}\, dx\, dy \tag{3}$$

where the region of integration corresponds to the projected cells of zone 1. By satisfying Eqs. (2) and (3), it can be shown that global conservation is enforced, i.e., the net integrated change in mass, momentum, and energy over a time step is equal to the summation of the physical boundary fluxes. The net contributions of the interface boundaries to the flux summations is identically zero.

It is assumed in practice that the grid spacing normal to the interface boundary is nominally the same between the zones to be patched. If the spacing is not the same, the error introduced is equivalent to that introduced into a single grid by a step discontinuity in the spacing. This approximation reduces the dimension of the interpolation implied by Eq. (3) by 1, to a form very much like Eq. (2). For equal spacing in the x direction, Eq. (3) becomes

$$\int \boldsymbol{Q}^{(1)}(x_{i+1})\, dy = \int \boldsymbol{Q}^{(2)}(x_l)\, dy \tag{4}$$

On the other hand, the flux in zone 1 could have been constructed from the flux in zone 2 through Eq. (2), in which case a projection of zone 2 cells into zone 1 would be necessary to compute the required flux. The time-flux constraint equation counterpart of Eq. (4) is then

$$\int \boldsymbol{Q}^{(1)}(x_i)\, dy = \int \boldsymbol{Q}^{(2)}(x_{l-1})\, dy \tag{5}$$

Ideally, Eqs. (2), (4), and (5) would be satisfied. However, any two of the three equations are sufficient to pass information between the zones. The approach that enforces Eq. (2) and either of Eqs. (4) or (5), as in the work of Rai,[1] Hessinius and Rai,[5] and Walters et al.,[2,3,8] is referred to as the spatial-flux conservation approach. The approach that enforces Eqs. (4) and (5) is referred to as the time-flux conservation approach. This latter approach satisfies Eq. (2), and hence global conservation, to within truncation error. Near a shock, the truncation error as derived from the Taylor series approximation is not appropriate, and, thus, the former approach is more attractive from a theoretical standpoint for capturing weak solutions to the governing equations. Nonetheless, the latter approach has been found, in practice, to maintain the conservative, i.e., shock-capturing, properties of the single-zone scheme.[7,8] The latter approach arises naturally in rezoning techniques for Lagrangian or adaptive-mesh simulations as well as in transferring information between grids in a multigrid calculation.

Viewing Eq. (3) as a conservative interpolation of the time fluxes at a projection of one zone into another, it is clear that the approach does not rely on the boundaries being coincident; hence, overlapped grids, such as those used in the Chimera scheme of Benek et al.,[4] can be accommodated. Also, the time-flux approach eliminates the departure from freestream conditions that can occur near curved interfaces using the spatial-flux approach because of the differences in the discrete boundary definitions of the two zones.[8]

For higher-order spatial differencing, the preceding equations need to be augmented with relations representing the additional information required at the interface. For a four-point stencil at the interface, such as used in the present work, a minimum of four interpolations need to be done at an interface using either the spatial-flux or the time-flux approach.

Interpolation Algorithms

The conservative interpolations implied previously can be evaluated discretely in a variety of ways. Defining $C_j^{(1)}$ as the discrete flux in zone 1 to be interpolated at a particular x position from the discrete flux in zone 2, $C_m^{(1)}$, Rai[1] has used a piecewise-constant projection of C from one grid onto the other, as

$$C_j^{(1)} = \sum_m C_m^{(2)} N_j^m \tag{6}$$

$$N_j^m = \begin{cases} 0, & \text{if } y_{m+1/2} < y_{j-1/2} \\ 0, & \text{if } y_{m-1/2} > y_{j+1/2} \\ \dfrac{1}{\Delta y_j} \displaystyle\int_{\max(y_{m-1/2},\, y_{j-1/2})}^{\min(y_{m+1/2},\, y_{j+1/2})} dy, & \text{otherwise} \end{cases} \tag{7}$$

The N_j^m represents the relative area of overlap of cell m onto the cell j, $0 \le N_j^m \le 1$, and the discrete flux balance is maintained, as

$$\sum_j C_j^{(1)} \Delta y_j = \sum_m C_m^{(2)} \Delta y_m$$

since $\Sigma_j N_j^m \Delta y_j = \Delta y_m = y_{m+1/2} - y_{m-1/2}$. The piecewise-constant approximation is, in general, only first-order accurate. Interpolating onto a coarse grid from a fine grid, the coarse-grid values can accurately represent the integrated average of the fine-grid solution. However, interpolating onto a fine grid from a coarse grid leads to the least accurate situation because the discrete fine-grid solution reflects the "stairstep" approximation of the coarse grid. This effect can be seen in the patched-grid inlet study of Ref. 7, where an oblique shock passes from a coarse grid into a much finer one. The virtue of the piecewise-constant projection is its simplicity and efficiency, especially in three-dimensional applications.

For second-order accuracy the distribution of flux in zone 2 can be taken as piecewise linear,

$$C^{(2)}(y) = C_m^{(2)} + (D_y C^{(2)})_m (y - y_m)$$

$$\text{for } y_{m-1/2} \le y \le y_{m+1/2} \tag{8}$$

where $(D_y C)_m$ represents the divided difference in zone m and can be determined to maintain monotonicity between adjacent zones.[16]

The projection of the zone 1 grid onto the zone 2 grid gives

$$C_j^{(1)} = \sum_m [C_m^{(2)} N_j^m + (D_y C^{(2)})_m M_j^m] \tag{9}$$

$$M_j^m = \begin{cases} 0, & \text{if } y_{m+1/2} < y_{j-1/2} \\ 0, & \text{if } y_{m-1/2} > y_{j+1/2} \\ \dfrac{1}{\Delta y_j} \displaystyle\int_{\max(y_{m-1/2},\, y_{j-1/2})}^{\min(y_{m+1/2},\, y_{j+1/2})} (y - y_m)\, dy, & \text{otherwise} \end{cases} \tag{10}$$

where the discrete flux balance is again maintained since $\Sigma_j M_j^m \Delta y_j = 0$. This approximation repairs the inaccuracy of the piecewise-constant integration when interpolating to finer grids from coarser grids.

An alternate method is to use a nonconservative pointwise interpolation to evaluate the flux, as from Eq. (8) evaluated at the cell centers of zone 2,

$$C_j^{(1)} = C^{(2)}(y_j) = C_m^{(2)} + (D_y C^{(2)})_m (y_j - y_m)$$

$$\text{for } y_{m-1/2} \le y_j \le y_{m+1/2} \tag{11}$$

The discrete conservation constraint equations are then satisfied only to within truncation error. The lack of complete conservation is most apparent when interpolating to a coarser mesh from a finer mesh, where the flux interpolated at the center of the coarse-grid zone may not be representative of an integrated value for the finer-grid flux over the extent of the coarser-grid zone. However, this limitation can be circumvented by imposing

$$C_j^{(1)} = \frac{1}{N} \sum_{p=1}^{N} C^{(1)}(y_p) \tag{12}$$

where $C^{(1)}(y_p)$ is defined pointwise from Eq. (8) evaluated at

$$y_p = y_{j-1/2} + [(2p - 1)/2N] \Delta y_j, \qquad p = 1, N \tag{13}$$

representing the cell centers resulting from a division of the coarse cell zone into N smaller zones. This correction need only be used when interpolating from fine cells onto coarse cells, so the N can be chosen automatically as, for example,

$$N = \max\left(1, \frac{y_{j+1/2} - y_{j-1/2}}{y_{m+1/2} - y_{m-1/2}}\right) \tag{14}$$

In the limit of $N \to \infty$, the procedure satisfies the conservative property exactly. Exact satisfaction of the conservation equations is a sufficient condition for capturing weak solutions to the governing equations, such as shocks and slip surfaces, although the computational evidence to date indicates that it is not a necessary condition. In regions of the flowfield where the variations in the flow are smooth, Eq. (11) is sufficient.

Surface Patching

The three-dimensional counterpart of the present zonal approach along a line in two dimensions (Fig. 1) corresponds to patching along a surface. Given the three-dimensional coordi-

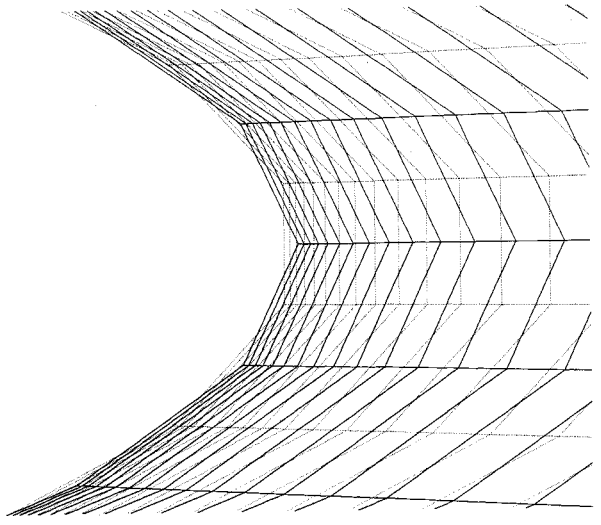

Fig. 2 Coincident zonal interface for zone 1 grid (solid lines) and for zone 2 grid (dotted lines) near partial boundary of ellipse.

nate transformation implied in Eq. (1) for each zone,

$$r = r(\xi,\eta,\zeta) \tag{15}$$

a patching surface can be defined without loss of generality as a surface of constant ξ. The patching algorithm must match the solution between the zones given the set of surface points on each grid defining the patching surface, as illustrated in Fig. 2 for a planar interface.

To interpolate across the interface, the transformation defined by the discrete ordered set of points in zone 1

$$\{r(\xi_i,\eta_j,\zeta_k) : i = i_{\max};\ j = 1, j_{\max};\ k = 1, k_{\max}\}$$

is used to construct the generalized coordinates at the patch interface ξ = const for the set of points in zone 2 corresponding to the patch boundary,

$$\{r(\eta_m,\zeta_n;\xi) : m = 1, m_{\max};\ n = 1, n_{\max}\}$$

The spatial-flux conservation of mass, momentum, and energy at the interface ξ = const is enforced by imposing

$$\int\int \hat{F}^{(1)}\, d\eta\, d\zeta = \int\int \hat{F}^{(2)}\, d\eta\, d\zeta \tag{16}$$

which is analogous to Eq. (2) for the two-dimensional case. Likewise, the three-dimensional counterpart to Eq. (3) is

$$\int\int\int \hat{Q}^{(1)}\, d\xi\, d\eta\, d\zeta = \int\int\int \hat{Q}^{(2)}\, d\xi\, d\eta\, d\zeta \tag{17}$$

where the limits of integration span the region encompassed by the projection of zone 1 cells. The spatial-flux conservation approach uses Eqs. (16) and (17) to patch across the boundary; the time-flux conservation approach uses Eq. (17) and an analogous equation for the projection of zone 2 into zone 1. The assumption of equal spacing across the interface reduces Eq. (17) to a two-dimensional equation.

Equations (16) and (17) express the conservation relations for the redistribution of flux on one side of the interface onto the cell faces of the grid opposite the interface. Assuming a piecewise-constant variation of the flux, the interpolation of the solution quantities across the interface is reduced to the determination of the area of overlap $N_{j,k}^{m,n}$ from the cell faces (m,n) of one zone onto the cell faces (j,k) of the other, i.e.,

$$C_{j,k}^{(1)} = \sum_m \sum_n C_{m,n}^{(2)}\, N_{j,k}^{m,n} \tag{18}$$

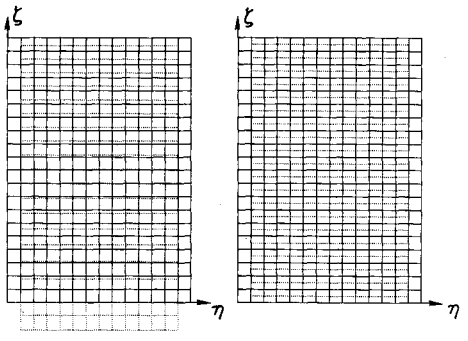

a) Bilinear basis **b) Biquadratic basis**

Fig. 3 Generalized coordinates of zone 2 cell center locations (dotted lines) in transformation defined by zone 1 grid (solid lines) for partial ellipse section.

One approach for determining the area of overlap is a clipping algorithm, adapted from computer graphics, which has been used in the three-dimensional zonal calculations of Refs. 2, 3, and 5. A more efficient procedure, originally developed for Lagrangian hydrodynamic rezoning calculations by Ramshaw,[17] relies on the divergence theorem applied to the position vector to calculate the area as summation of line integrals over the bounding polygons. For a linear mapping of the surface

$$r = a_1 + a_2\eta + a_3\zeta \tag{19}$$

the area A_p of a cell face bounded by s directed line segments running from (η_1,ζ_1) to (η_2,ζ_2) is

$$A_p = \frac{|a_2 \times a_3|}{2} \sum_s \epsilon_s^p\, (\eta_1\zeta_2 - \eta_2\zeta_1) \tag{20}$$

where ϵ_s^p is either $+1$ or -1 as the cell p lies to the left or right, respectively, of the line segment s. The areas of overlap can be calculated by sweeping over the line segments of the two meshes because all of the areas of overlap are formed by the intersection of mesh lines on the two surfaces. This procedure has been used in the three-dimensional calculations of Kathong et al.,[6] Walters et al.,[3] and Ghaffari et al.[10] The computational work for the area of overlap scales linearly with the number of mesh points. In a straightforward application, this procedure is more efficient than the clipping approach.[3]

The procedure used in most of the calculations reported here is to interpolate to the cell centers of one grid assuming a linear variation of the flux within the cells of the other grid, as

$$C_{j,k}^{(1)} = C_{m,n}^{(2)} + (D_\eta C^{(2)})_{m,n}\,(\eta_j - \eta_m) + (D_\zeta C^{(2)})_{m,n}\,(\zeta_k - \zeta_n)$$

$$\text{for } \eta_{m-1/2} \le \eta_j \le \eta_{m+1/2},\ \zeta_{n-1/2} \le \zeta_k \le \zeta_{n+1/2} \tag{21}$$

analogously to Eq. (11) in the two-dimensional case. For both approaches, the geometric information describing the interpolation from one zone to another is calculated initially and then reused at each subsequent iteration so that the additional overhead due to the patching is minimal.

To construct the generalized coordinates of one zone given the discrete transformation defined by another zone, a local geometric variation is assumed in each cell. A bilinear variation in each cell

$$r = a_1 + a_2\eta + a_3\zeta + a_4\eta\zeta \tag{22}$$

leads to a mismatch in the discrete boundary definition between the two grids near a curved boundary, as illustrated in Fig. 2. The boundary mismatch is not generally an issue for

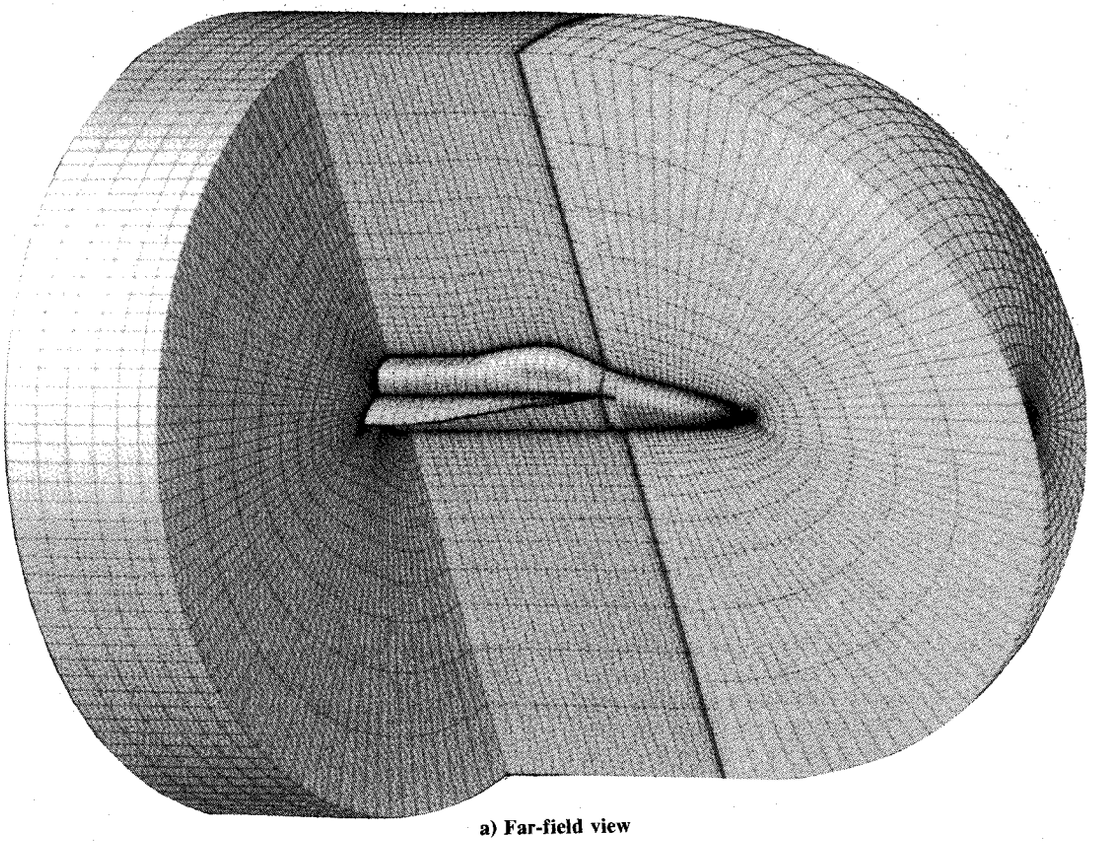

a) Far-field view

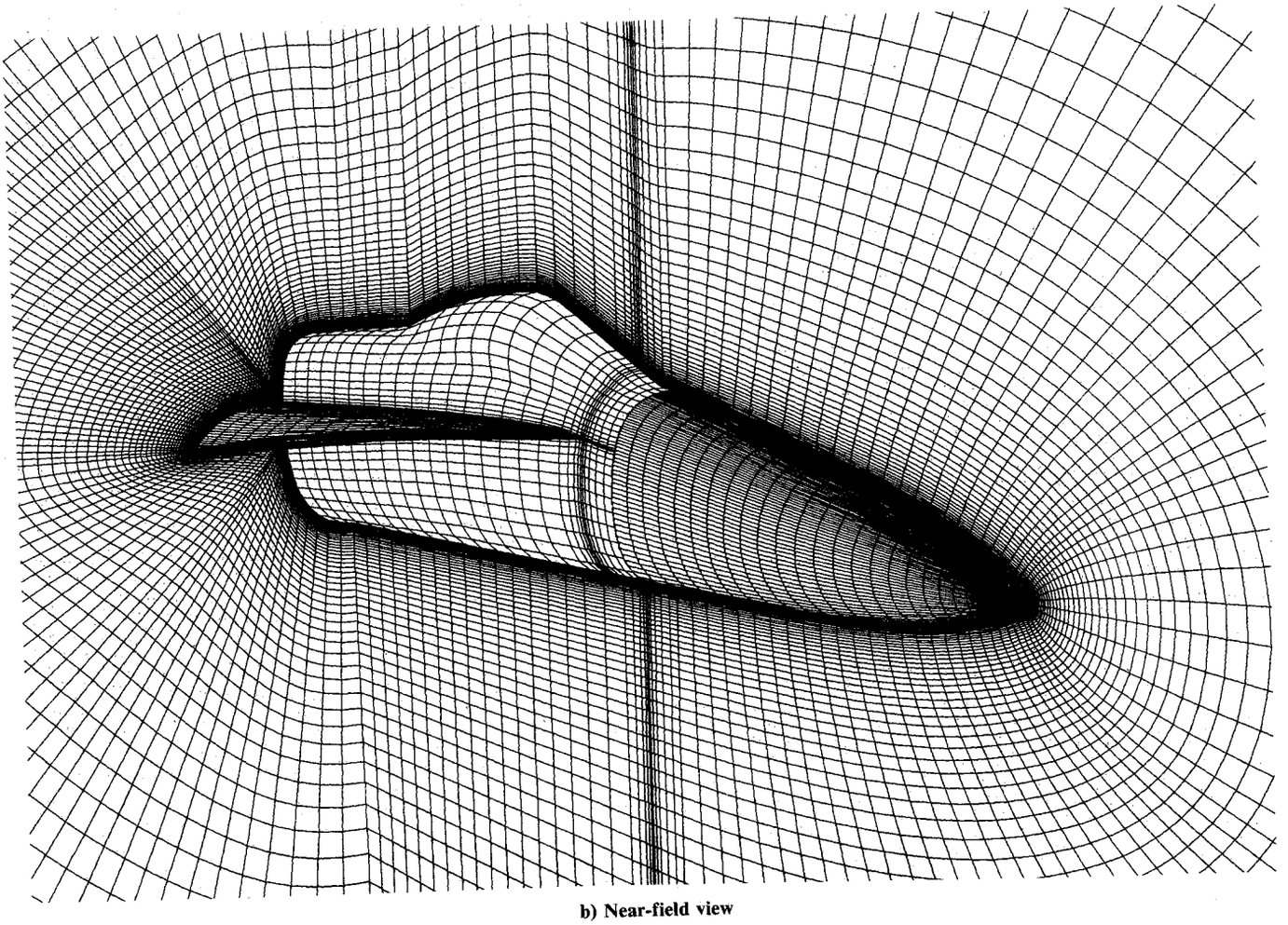

b) Near-field view

Fig. 4 F/A-18 forebody-LEX three-block grid.

meshes encountered in computations for the Euler equations because the mismatch is a small fraction of the area of the cells adjacent to the boundary. For solutions to the Navier-Stokes equations, in which the grids are highly clustered near the boundary to resolve the viscous layers at high Reynolds numbers, the situation depicted in Fig. 2 is not uncommon. In Fig. 3a, the cell centers of one zone are shown in the generalized coordinate frame of the other zone (unit spacing in η and ζ); the two cell centers nearest the boundary actually lie outside the discrete boundary of the other zone. For the zones shown, the physical grid spacing normal to the boundary is the same for both zones and, in the outer part of the grid, the cell centers lie midway between the grid lines, as expected.

The surface definition can be substantially improved by using a biquadratic fit, i.e.,

$$r = a_1 + a_2\eta + a_3\zeta + a_4\eta\zeta + a_5\eta^2 + a_6\eta^2\zeta + a_7\eta\zeta^2 + a_8\zeta^2 \quad (23)$$

This form ensures that the boundaries of the cells in a zone are continuous if the grid point data are augmented by additional points at the centers of the interface. These additional points are determined by passing a least squares quadratic curve through the two grid points defining a cell edge and the nearest grid point on either side. The generalized coordinates of each cell center to be interpolated are determined through a nonlinear iterative procedure. A nearest enclosing cell is guessed based on the distance from the grid point data to the cell center and then updated by solving for (η,ζ) from Eq. (23) through a Newton procedure, until the computed (η,ζ) lies within the candidate cell boundary. A degenerate fit ($a_7 = a_8 = 0$) is sufficient for the grids considered here. The conserved variables are then interpolated using the linear fit of Eq. (21).

For the zones in Fig. 2, the grid mismatch near the boundary is reduced from $\mathcal{O}(1)$ to $\mathcal{O}(10^{-2})$, as shown in Fig. 3b, wherein all the cell centers lie very close to midway between the grid points of the other. For highly stretched meshes with widely disparate physical spacing in both the tangential and normal directions, even the biquadratic fit is insufficient. In those extreme cases, a local interpolation at the boundary based on tangential and relative normal distance from the boundary has been found to be sufficient.

Computational Results

A three-block grid, shown in Fig. 4, is described below. The grids in each block are generated independently using transfinite interpolation. The upstream block is a C-O topology, which leads to an efficient resolution of the forebody geometry; the grid points are clustered circumferentially in the leeward region. Two additional blocks, one ahead of the leading-edge-extension (LEX) apex and one behind, with an H-O topology are located downstream of the first block. The LEX geometry is extended in the computation $1\bar{c}$ downstream of the approximate physical position where the LEX intersects the wing on the actual F/A-18. Two zonal interfaces are required and the methodology allows disparate spacing at the zonal interface, which is evident in Fig. 4a on the body surface and in the longitudinal plane of symmetry at the first interface. The near-field view in Fig. 4b shows the actual grid used for the turbulent computations shown below and illustrates a circumferential clustering on the upper surface of the LEX surface. Each of the three blocks has 73 points in the normal direction with the same stretching rate, and, thus, the only interface grid discontinuity that shows in Fig. 4b is along the circumferential direction at the first zonal interface. The spacing normal to the surface is $2 \times 10^{-5}\bar{c}$ at the surface, which corresponds to a $y^+ \approx 5$ for the turbulent flow computations at flight Reynolds number. A total of 360,255 grid points are used in the computation, of which 4935 define the forebody-LEX geometry.

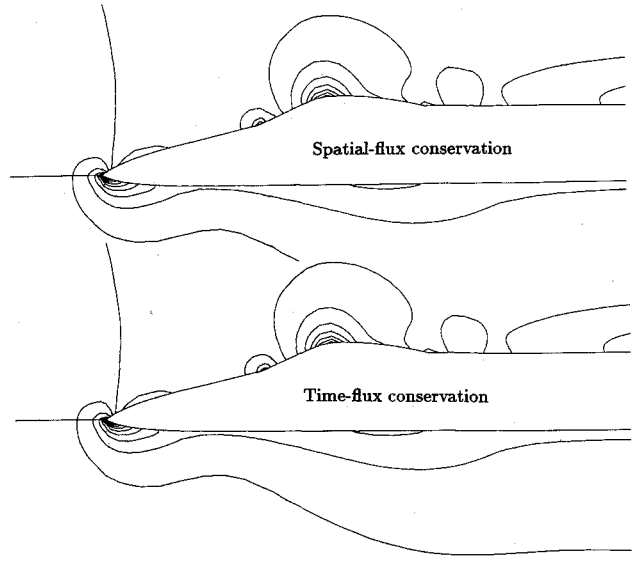

Fig. 5 Longitudinal symmetry plane pressure contours; $M_\infty = 0.6$, $R_{\bar{c}} = 0.8 \times 10^6$, $\alpha = 20$ deg.

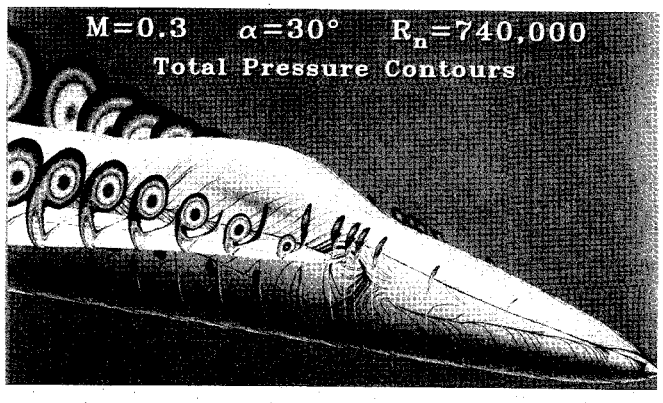

Fig. 6 Total pressure contours and surface particle traces; two-block grid, $M_\infty = 0.3$, $R_{\bar{c}} = 0.74 \times 10^6$, $\alpha = 30$ deg.

A two-zone grid is used for the laminar computations reported here and is described in detail by Ghaffari et al.[10] Both blocks have an H-O topology and are patched together at the LEX apex.

Laminar Flow Computations

Symmetry plane pressure contours using the spatial-flux conservation strategies for the two-block grid are shown in Fig. 5 for the conditions considered in detail by Ghaffari et al.[10]: $M_\infty = 0.6$, $R_{\bar{c}} = 0.8 \times 10^6$, $\alpha = 20$ deg. Both calculations interpolate across the zonal interfaces using the piecewise-constant Ramshaw algorithm, Eqs. (18) and (29). The two solutions are nominally the same; any differences are on the order of the truncation error of the calculations.

Computed total pressure contours and surface particle traces are shown in Fig. 6 at a high angle-of-attack, laminar flow condition: $M_\infty = 0.3$, $R_{\bar{c}} = 0.74 \times 10^6$, $\alpha = 30$ deg. The primary and secondary separation lines on the forebody are evident, as well as the secondary separation line on the LEX. The vortices shed along these lines are very shallow and lie close to the body surface, especially in comparison to the primary vortex shed from the LEX. The primary separation line on the forebody leads into a large region of reverse flow ahead of and predominantly under the LEX apex. Under the LEX along the body, a primary separation line is evident, leading to a vortex impinging on the LEX lower surface. Along the fuselage above the LEX, a separation line extending downstream from the apex is evident. The streamlines pass smoothly through the zonal interfaces. The overall flowfield is

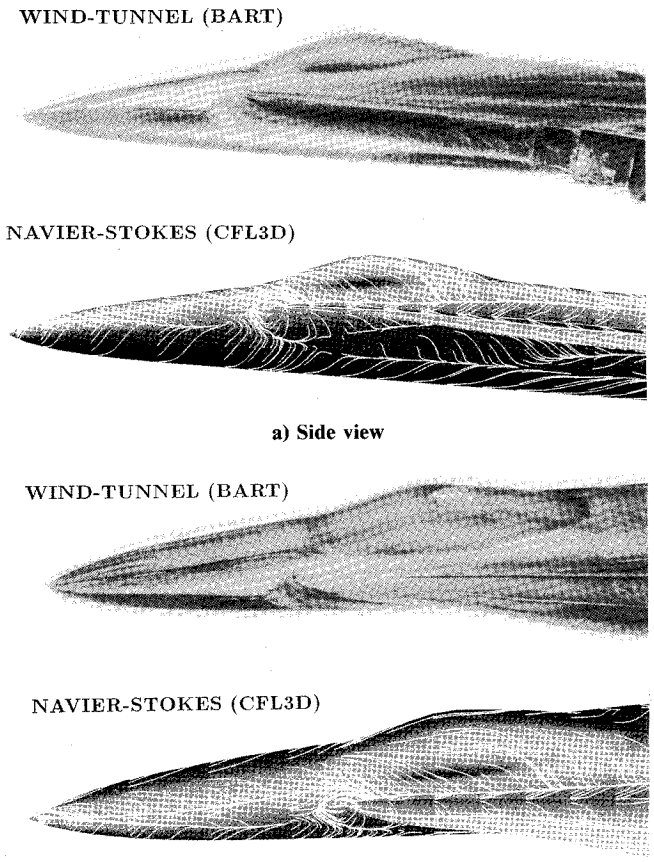

Fig. 7 Wind-tunnel (top) and computed (bottom) surface flow patterns at low-speed, laminar flow conditions; $\alpha = 30$ deg.

qualitatively similar to the laminar calculations given by Ghaffari et al.[10] at $\alpha = 20$ deg.

Oil flows from a test in the Basic Aerodynamics Research Tunnel (BART)[18] at NASA Langley Research Center for the same angle of attack but slightly lower Reynolds number, $R_{\bar{c}} = 0.2 \times 10^6$, are compared to the computed particle traces in Fig. 7. The experimental oil flows demonstrate a striking agreement with the computations in the position of primary and secondary separation lines on the forebody and LEX, as well as in the extent of separated flow underneath the LEX.

Turbulent Flow Computations

Wind-tunnel results at higher Reynolds numbers and in-flight results show markedly different surface flow patterns[9] from Fig. 7. The flight-test results correspond to a Reynolds number of $10\text{–}15 \times 10^6$ based on $\bar{c}$ and show primary and secondary separation lines on the forebody much closer to the leeward plane of symmetry. Computed particle traces at flight Reynolds number for the three-block grid of Fig. 4 are compared with the flight-test results[19] in Fig. 8. The interface interpolations were done with the time-flux approach, using Eq. (23) and the generalized coordinate interpolations of Eq. (21). The surface flow passes smoothly through the two zonal interfaces. The first zonal interface has a significant variation in the circumferential spacing of the grid on either side, and the improved interpolation obtained with the biquadratic fit to the surface geometry is critical in obtaining the smooth results shown.

The computed primary and secondary separation lines on the forebody are extremely well predicted in comparison to flight. In comparison to the laminar flow results, Fig. 7, the extent of separation in the LEX apex region is considerably reduced and the secondary separation line on the LEX is

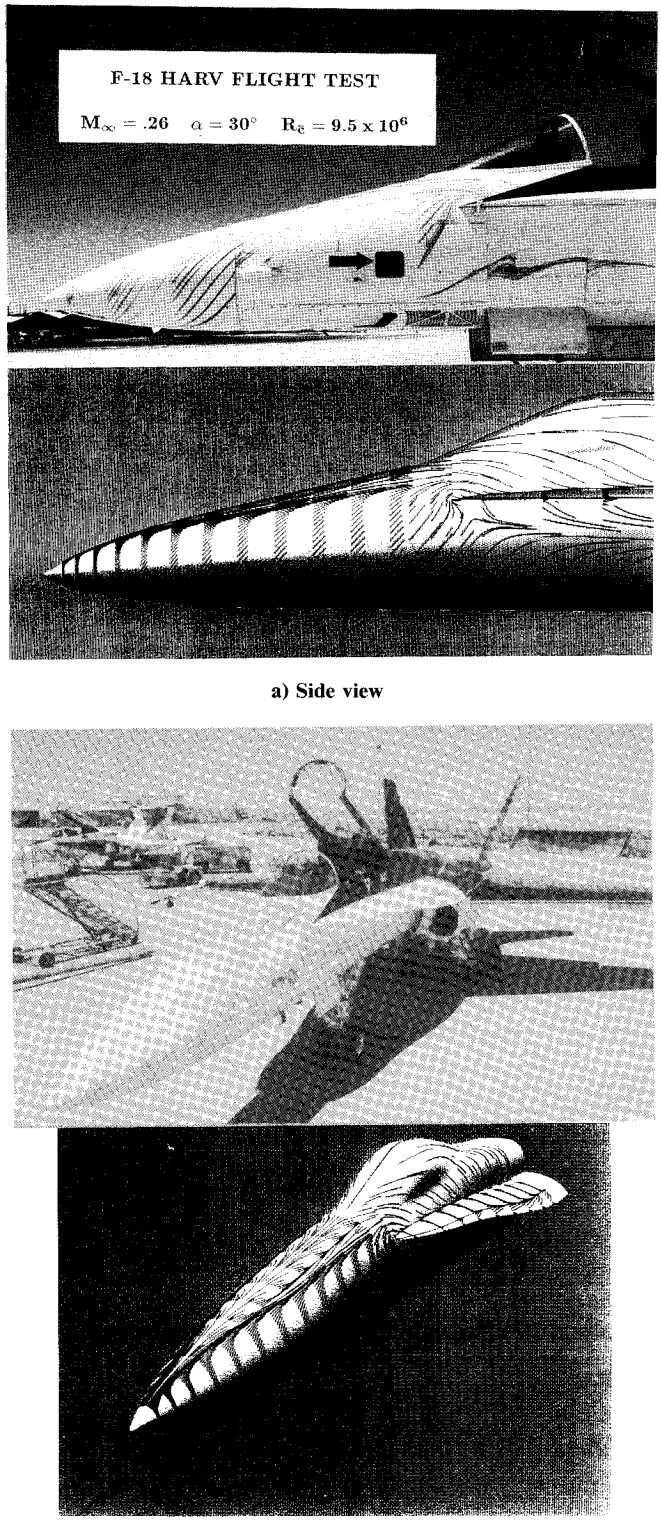

Fig. 8 Flight-test (top) and computed (bottom) surface flows; $M_\infty \approx 0.3$, $R_{\bar{c}} \approx 10 \times 10^6$, $\alpha = 30$ deg.

moved outward in both computation and experiment, as expected. Detail inspection of the flight-test results indicate that both secondary and tertiary separation lines are evident in the LEX region; the tertiary separation line appears to merge with the secondary line near the leading edge of the wing. A single secondary separation line is predicted in the computations on the LEX and is in close agreement with the position of the secondary separation line from the flight oil flow. The agreement shown is encouraging, in light of the fact that only the

forward portion of the complete configuration is being modeled.

Concluding Remarks

A patched-grid algorithm for complex configurations has been described. The effort is an extension to the longitudinally patched approach of Refs. 2 and 3, allowing for the analysis of grids that are highly stretched in the normal direction to resolve viscous flows and for arbitrarily shaped patch surfaces. Two algorithms, a spatial-flux and a time-flux conservation approach, have been used across zonal interfaces with few differences noted. The latter approach is somewhat more flexible and can be easily extended to handle more complex situations, such as overlapped and embedded grids.

Applications using the algorithm have been made to the F/A-18 forebody-LEX configuration at $\alpha = 30$ deg over a range of Reynolds number. The laminar flow calculations agree well with oil flow results from wind-tunnel tests at $R_{\bar{c}} = 0.2 \times 10^6$. The turbulent flow calculations predict primary and secondary separation lines on the forebody close to the leeward plane of symmetry that agree well with flight-test results at $R_{\bar{c}} = 10 \times 10^6$. The wind-tunnel results at $R_{\bar{c}} \approx 1 \times 10^6$ exhibit a separation pattern different from either calculation[9]; the difference can be attributed to a transition from laminar to turbulent flow. A laminar separation bubble, experimentally visualized,[9] occurs in the region of the primary separation line predicted by the present method, assuming a laminar viscous model.

Acknowledgments

NASA Langley Research Center sponsored the work of the second and third authors under NASA Grant NAG1-866 and that of the fourth author under NASA Contract NAS1-17919. The authors wish to thank Scott Kjelgaard of NASA Langley Research Center for providing the flow visualizations of the F/A-18 configuration in BART and Dave Fisher of the NASA Dryden Flight Research Facility for providing surface flow visualization photographs of the NASA F/A-18 HARV along with supporting flight data.

References

[1]Rai, M. M., "A Relaxation Approach to Patched-Grid Calculations with the Euler Equations," AIAA Paper 85-0295, Jan. 1985.

[2]Walters, R. W., Reu, T., McGrory, W. D., Thomas, J. L., and Richardson, R. F., "A Longitudinally-Patched Grid Approach with Applications to High Speed Flows," AIAA Paper 88-0715, Jan. 1988.

[3]Walters, R. W., Reu, T., Thomas, J. L., and McGrory, W. D., "Zonal Techniques for Flowfield Simulation about Aircraft," *Computers and Structures*, Vol. 30, No. 1 1988, pp. 47–54.

[4]Benek, J. A., Buning, P. G., and Steger, J. L., "A 3-D Chimera Grid Embedding Technique," AIAA Paper 85-1523, July 1985.

[5]Hessinius, K. A., and Rai, M. M., "Three Dimensional, Conservative, Euler Computations Using Patched Grid Systems and Explicit Methods," AIAA Paper 86-1081, May 1986.

[6]Kathong, M., Smith, R. E., and Tiwari, S. N., "A Conservative Approach for Flow Field Calculations on Multiple Grids," AIAA Paper 88-0224, Jan. 1988.

[7]Thomas, J. L., Rudy, D. H., Chakravarthy, S. R., and Walters, R. W., "Patched Grid Computations of High Speed Inlet Flows," *Advances and Applications in Computational Fluid Dynamics*, Vol. 66, Nov.–Dec., 1988, pp. 11–22.

[8]Walters, R. W., Thomas, J. L., and Switzer, G. F., "Aspects and Applications of Patched Grid Calculations," AIAA Paper 86-1063, May 1986.

[9]Fisher, D. F., Richwine, D. M., and Banks, D. W., "Surface Flow Visualization of Separated Flows on the Forebody of an F-18 Aircraft and Wind-Tunnel Model," NASA TM 100436, 1988.

[10]Ghaffari, F., Luckring, J. M., Thomas, J. L., and Bates, B. L., "Navier-Stokes Solutions About the F/A-18 Forebody-LEX Configuration," AIAA Paper 89-0338, 1989.

[11]Baldwin, B. S., and Lomax, H., "Thin Layer Approximation and Algebraic Model for Separated Turbulent Flows," AIAA Paper 78-257, 1978.

[12]Degani, D., and Schiff, L. B., "Computation of Supersonic Viscous Flows Around Pointed Bodies at Large Incidence," AIAA Paper 83-0034, Jan. 1983.

[13]Vatsa, V. N., Thomas, J. L., and Wedan, B. W., "Navier-Stokes Computations of a Prolate Spheroid at Angle of Attack," *Journal of Aircraft*, Vol. 26, No. 11, 1989, pp. 986–993.

[14]Thomas, J. L., Taylor, S. L., and Anderson, W. K., "Navier-Stokes Computations of Vortical Flows Over Low Aspect Ratio Wings," AIAA Paper 87-0207, Jan. 1987.

[15]Van Leer, B., Thomas, J. L., Roe, P. L., and Newsome, R. W., "A Comparison of Numerical Flux Formulas for the Euler and Navier-Stokes Equations," AIAA Paper 87-1104, June 1987.

[16]Van Leer, B., "Upwind-Difference Methods for Aerodynamic Flows Governed by the Euler Equations," *Lectures in Applied Mathematics*, Vol. 23, Pt. 2, Academy of Military Science, Providence, RI, 1985, pp. 327–336.

[17]Ramshaw, J. D., "Conservative Rezoning Algorithms for Generalized Two-Dimensional Meshes," *Journal of Computational Physics*, Vol. 59, 1985, pp. 193–199.

[18]Sellers, W. L., III, and Kjelgaard, S. O., "The Basic Aerodynamics Research Tunnel—A Facility Dedicated to Code Validation," AIAA Paper 88-1997, May 1988.

[19]Fisher, D. F., and Meyer, R. R., Jr., "Flow Visualization Techniques for Flight Research," NASA TM-100455, Oct. 1988.